10.4 THREE-DIMENSIONAL CHARACTERISTICS OF MOUNTAIN WAVES GENERATED BY THE SIERRA NEVADA

James D. Doyle[1], Ronald B. Smith[2], William A. Cooper[3], Vanda Grubišić[4], Jorgen Jensen[3], Qingfang Jiang[5]

[1]*Naval Research Laboratory, Monterey, CA*
[2]*Yale University, New Haven, CT*
[3]*NCAR/UCAR, Boulder, CO*
[4]*DRI, Reno, NV*
[5]*UCAR, Monterey, CA*

1. INTRODUCTION

The Sierra Nevada mountain range is a north-northwest to south-southeast oriented mountain range of approximately 650 km length, 100 km width, and features the tallest peak, Mt. Whitney (4,417 m), and the steepest orographic gradient along the eastern slope in the contiguous United States (Fig. 1a). The Sierra Nevada is well known for generating large amplitude mountain waves (i.e., the Sierra Wave). Although the Sierra Nevada is often considered nearly a two-dimensional barrier to southwesterly flow, the range has a number of peaks above 4 km along the crest and several deep passes as shown in Fig. 1b.

Investigations of constant wind speed and static stability flow past elongated three-dimensional (3-D) mountains suggest that the response can differ significantly relative to flow over 2-D ridges (e.g., Epifanio and Durran 2001). Flow splitting, vortex shedding, and wakes are examples of phenomena that may occur in stratified flows past 3-D obstacles (e.g. Smolarkiewicz and Rotunno 1989; Schär and Durran 1997). Likewise, the palette of gravity wave responses is quite complex for stratified flow over 3-D mountains, with hydrostatic, nonhydrostatic, and inertia-gravity waves all possible.

Measurements from the NSF/NCAR High-performance Instrumented Airborne Platform for Environmental Research (HIAPER) obtained during the recent Terrain-Induced Rotor Experiment (T-REX) (Grubišić et al. 2004) indicate marked differences in the character of the wave response between northern and southern cross Sierra tracks, which were separated by a distance of approximately 50 km. Multiple racetracks at several stratospheric altitudes indicate that these differences were repeatable, which is suggestive that the deviations were likely due to mountain waves that varied systematically in amplitude rather than associated with transients. Some research flights indicated that the largest variations were on the northern flight leg, while larger variations were occasional encountered on the southern leg. The topography beneath the northern segments is typically higher than the southern segment. However, a number of topographic peaks near the southern segment are among the highest in the Sierra (Fig. 1b)

Corresponding Author Address: James D. Doyle, NRL, 7 Grace Hopper Ave., Monterey, CA 93943-5502; doyle@nrlmry.navy.mil

In this study, we make use of the HIAPER observations along with nonhydrostatic numerical model simulations and linear theory to test the hypothesis that terrain variations in the height of the Sierra crest and lee side slopes are responsible for variability in the wave amplitude and characteristics in the along-barrier direction.

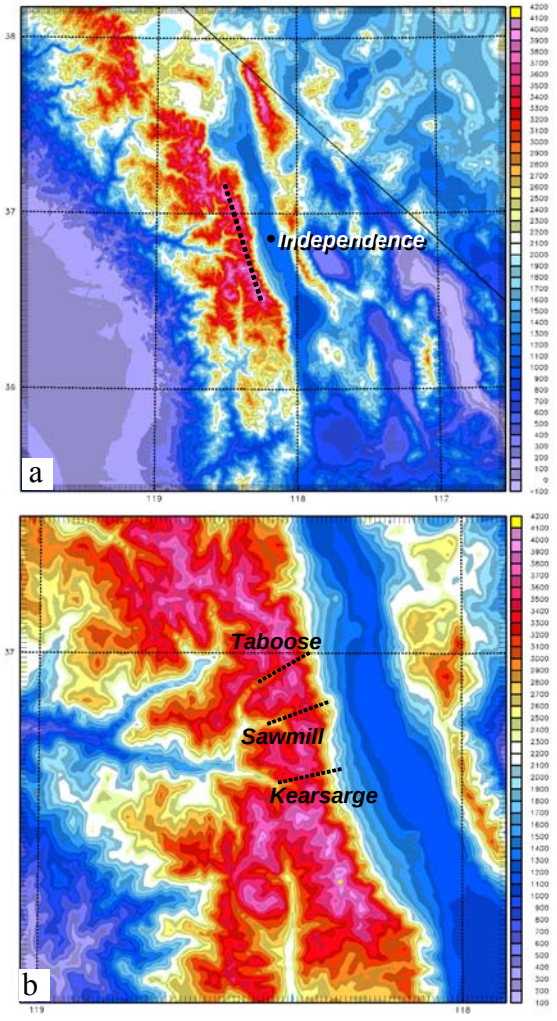

Fig. 1. Terrain height (m) for the (a) Sierra Nevada and (b) T-REX observation region showing high passes.

2. T-REX AND HIAPER OVERVIEW

The overarching objective of the Terrain-induced Rotor Experiment (T-REX) is explore rotor and mountain wave dynamics and study the synergistic interaction between rotors, mountain waves, and boundary layer dynamics (Grubišić et al. 2004). One of the objectives of T-REX is to gain a better understanding of mountain wave dynamics including the characteristics of wave launching, propagation, and breakdown. The observing period of T-REX took place in March-April 2006 and featured 15 Intensive Observation Periods (IOPs) including 12 HIAPER flights, as summarized in Table 1.

The HIAPER GV platform was instrumented with basic *in situ* measurement capabilities for the flights during T-REX. The instruments included a gust probe system, static pressure, fast temperature probe, fast tracer system including water vapor, ozone, CO, and condensation nuclei. The aircraft was also equipped with cameras and a differential GPS that enables very accurate determination of the geographic location and altitude. A GPS dropwindsonde system was onboard HIAPER and more than 300 sondes were deployed (Table 1).

The T-REX HIAPER observational strategy consisted of long racetracks to deduce 3-D aspects of the wave field and compute circulation statistics. This also allowed for upstream and downstream regions to be compared. Multiple racetrack stacks spanning 4 km in altitude were designed to observe how the waves change as they propagate upward into the stratosphere. The racetracks were immediately repeated, as the conditions dictated, to document the steadiness of the rapidly changing wave fields. On each flight, deep aircraft soundings were performed to document the chemistry and basic properties of troposphere and lower stratosphere. The timing of the HIAPER missions was based on mountain wave activity forecasts from several numerical models including the 2-km resolution Coupled Ocean /Atmosphere Mesoscale Prediction System (COAMPS® Hodur 1997) and the 4-km resolution Weather Research and Forecasting (WRF) model.

IOP	Flight	Date	Track	700 mb Wind (m s^{-1} and dir)	Levels (Kft)	Drops	W_{max} (m s^{-1})
1	1	02 March	B	15 @ 240°	41, 43, 37, 32	17	1.5
2	2	05 March	C	15 @ 210°	41, 43, 37, 30	18	1.5
3	3	09 March	A	14 @ 280°	41, 43, 37, 30, 47	12	10
4	4	14 March	B	15 @ 250°	41, 43, 37, 30	31	6
6	5	25 March	B	17 @ 250°	40, 43, 39 ,37, 33	32	12
9	6	02 April	B	14 @ 230°	45, 43, 40, 37, 30	33	2
Inter.	7	06 April					
10	8	08 April	B	09 @ 235°	45, 43, 40, 37, 30	31	4
13	9	15 April	B	15 @ 260°	45, 43, 37, 30	37	2.5
13	10	16 April	B	13 @ 230°	45, 43, 37, 30	39	10
14	11	21 April	C	10 @ 180°	43, 40, 37, 33, 30	21	1.5
15	12	26 April	B	10 @ 040°	43, 40, 37, 33, 30	43	2

Table 1. Summary of the T-REX HIAPER flights.

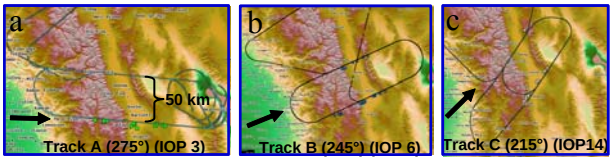

Fig. 2. Prototypical HIAPER flight paths for a) Track A (IOP 3) oriented along 275°, b) Track B (IOP 6) oriented along 245°, and Track C (IOP 14) oriented along 215°.

3. HIAPER OBSERVATIONS OF THREE-DIMENSIONAL MOUNTAIN WAVES

The largest amplitude mountain waves observed by HIAPER occurred during the flights of IOP 4 (14 March), IOP 6 (25 March), and IOP 13 (16 April). The maximum vertical velocity observed by the aircraft was over 10 m s^{-1} in each of these flights. All three flights made use of flight track B oriented along 245°, nearly parallel to the large-scale flow. These three IOPs are ideal to contrast the mountain wave characteristics along the northern and southern flight segments, which were 50 km apart.

3a. Flight-Level Observations

A large-scale trough approached the U.S. West Coast and strong southwesterly flow impinged on the Sierra Nevada Range on 14 March during IOP 4. A HIAPER flight was executed along track B. A summary of the flight level data from the 13.1 km level for the 4 northern and southern flight segments are shown in Figs. 3a and 3b. There are a number of gross similarities between the northern and southern flight segments in IOP 4. For example, large amplitude waves in the lower stratosphere are apparent in both sections with maximum vertical velocities in excess of 6 m s^{-1} and potential temperature perturbations greater than 10 K. However, clearly there are a number of differences between the sections. The maximum wind speed and potential temperature perturbations are 15 m/s and 18 K, respectively, along the northern section and 20 m/s and 16 K along the southern route. The primary vertical velocity wave signature has a longer wavelength to the north and shorter to the south. The wave amplitude (crest to trough) is 12 m s^{-1} to the south and 6 m s^{-1} to the north. In the lee of the primary wave, short, small-amplitude, unsteady waves are present to the north, in contrast to the south where larger amplitude and somewhat more steady waves are apparent. The strongest descent occurs above the Inyo Range in the northern segment and in the mid-Owens Valley to the south. The southern section contains at least three short and small-amplitude waves upstream of the primary wave, while little wave activity is apparent in the northern segment

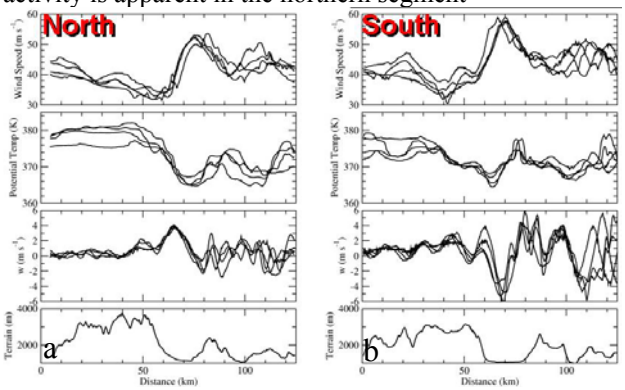

Fig. 3. Flight-level data at 13.1 km on 14 March (IOP 4). The wind speed (m s^{-1}, top panel), θ (K, second panel), w (m s^{-1}, third panel) and terrain (m, bottom panel) for the (a) northern and (b) southern flight segments are shown.

A second case considered here is IOP 6, which took place on 25 March 2006. This event featured very strong cross Sierra flow associated with a large-scale trough and a mid-tropospheric short-wave. In many respects, IOP 6 was the most intense event measured during T-REX. Once again the mountain wave characteristics over the northern and southern sections were quite different as illustrated by the flight level data for 13.1 km shown in Figs. 4a and 4b. The wave amplitude is larger on the southern legs than the northern and the wave structures appear to be more steady and repeatable. The perturbation potential temperature is 50% larger on the southern section than the northern leg. Likewise, the crest to trough maximum vertical velocity is 18 m s^{-1} for the southern leg and 13 m s^{-1} for the northern leg. Note that in both of the segments, the first strong downward vertical velocity "plunge" is displaced away from the highest terrain and lee slopes likely due to nonlinear effects.

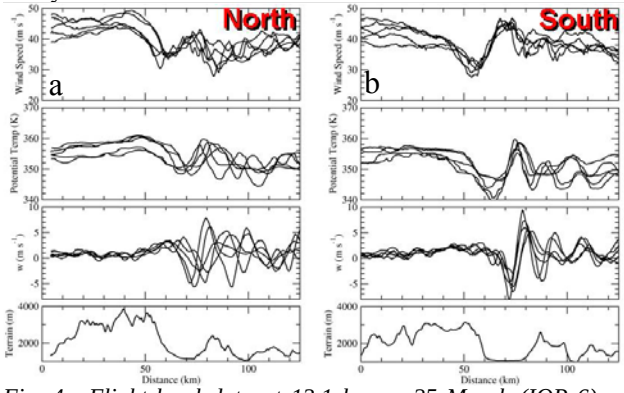

Fig. 4. Flight-level data at 13.1 km on 25 March (IOP 6). The wind speed (m s^{-1}, top panel), potential temperature (K, second panel), vertical velocity (m s^{-1}, third panel) and terrain interpolated to the flight path (m, bottom panel) for the (a) northern and (b) southern flight segments.

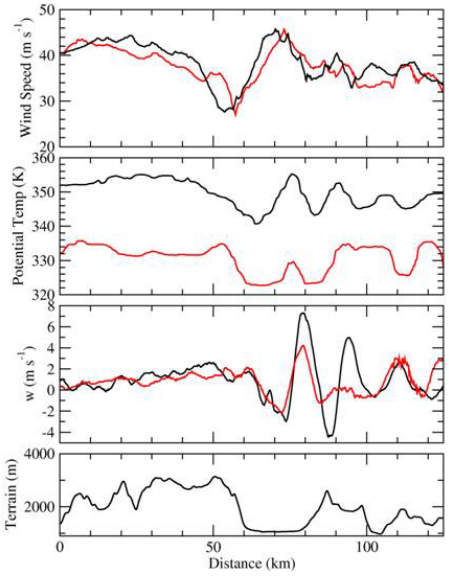

Fig. 5. Flight-level data at 13.1 (black) and 11.9 km (red) for two IOP 6 flight segments separated by a 30 min. interval.

The wave amplitudes for both segments showed significant differences at lower levels. In IOP 6 and a number of other events, the vertical velocity and wave amplitudes were largest in the highest levels in the stratosphere that were measured. For example, Fig. 5 shows data from two southern flight segments during IOP 6, which were separated by only 30 min. Much larger vertical velocities were present at 13.1 km than at 11.9 km, perhaps related to the decrease of density with height and background shear effects.

The final HIAPER flight leg for IOP 6 was flown at 45 kft (13.7 km) over the southern portion of the B racetrack. A large amplitude wave was encountered on this segment, as shown in Fig. 6. The perturbation wind speed and potential temperature was 35 m s^{-1} and 30 K, respectively, and the wavelength of this wave was quite large. The vertical velocity time series shows a broad downward directed minimum followed by a very sharp upward vertical velocity spike of 12 m s^{-1} (18 m s^{-1} in the high-rate dataset). It is noteworthy that the aircraft experienced rather strong turbulence during this encounter with the sharp vertical velocity. The location of the strongest ascent was well east of the Sierra slopes, perhaps once again attributable to nonlinear effects. The potential temperature measurements do not indicate a response to the sharp upward vertical velocity; however, a small-amplitude wind speed spike is apparent. A sharp ozone concentration maximum of 500 ppb, which is 350 ppb greater than the ambient background values, occurred nearly coincident with the vertical velocity maximum. The ozone maximum undoubtedly is related to advection of higher ozone concentration from other levels. Unfortunately, companion measurements along the northern section at 13.7 km were not performed. The wave amplitudes were significantly larger on the southern section at 13.1 km.

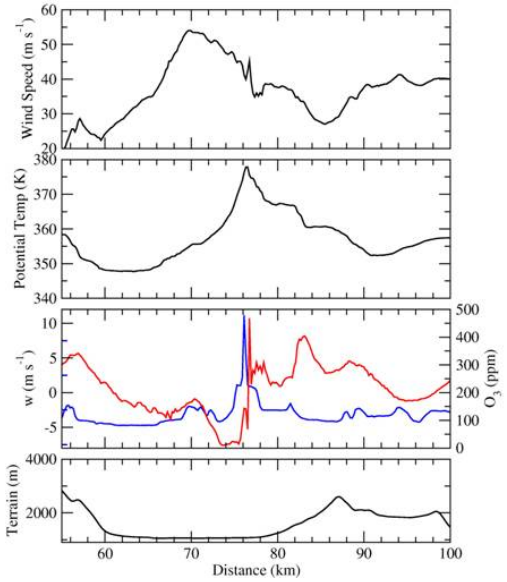

Fig. 6. Flight-level data at 13.7 for IOP 6 along a segment of a southern leg. The vertical velocity (m s^{-1}) is shown by the red in the third panel and ozone (ppb) in blue.

During T-REX, the strongest cross-Sierra flow at crest level occurred during IOP 13 on 15 April 2006 associated with a large-amplitude mid-tropospheric trough and jet stream synoptic-scale system. The HIAPER flight-level data for the northern and southern legs at 13.1 and 11.3 km are shown in Figs. 7a and 7b. The largest amplitude waves were observed at the 11.3 km level, in contrast to IOP 6. The short wavelength unsteady mountain waves are apparent downstream in the southern segment, unlike IOP 4 that featured similar characteristics along the northern segment (Fig. 3). The largest amplitude waves at 13.1 km in terms of vertical velocity occur along the northern flight segment, in contrast to IOP 4 and IOP 6.

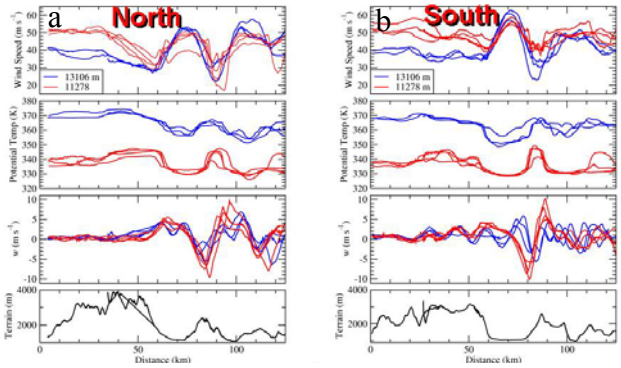

Fig. 7. Flight-level data at 13.1 km (blue) and 11.3 (red) on 15 April (IOP 13). The wind speed (m s^{-1}, top panel), potential temperature (K, second panel), vertical velocity (m s^{-1}, third panel) and terrain interpolated to the flight path (m, bottom panel) for the (a) northern and (b) southern flight segments.

3b. Vertical Velocity Spectra

The vertical velocity variance spectrum was computed for each HIAPER research flight leg at a number of different altitudes. In general, significant differences exist in the vertical velocity variance spectra along the northern and southern legs. To illustrate these differences, the vertical velocity variance spectrum at 13.1 km for IOPs 4 and 6 are shown in Figs. 8a and 8b. The terrain spectrum (bottom panels) shows marked differences between the southern and northern flight segments. The northern legs show a primary maximum in the terrain power spectrum near 30 km and a secondary maximum at 16 km. The southern legs exhibit a power spectrum maximum at wavelengths greater than 50 km and several secondary maxima at 21, 16 and 12 km.

The vertical velocity power spectrum for the southern legs appear to exhibit more energy at shorter wavelengths than for the northern segment. In the IOP 4 case, well defined maxima exist at 18-22 km wavelengths for the southern legs. The northern legs show considerably more variability exists with a primary wavelength of 42 km, secondary maxima at 20 and 30 km, and several additional small-amplitude maxima at wavelengths less than 15 km. The spectra for IOP 6 exhibit more well defined maxima for the northern segments with the power spectrum maximum occurring in the 16-22 km wavelength range. Power spectrum maxima occur at wavelengths of 16 km or less for the southern legs, with the exception of one leg that exhibited a peak at 22 km. Finally, it should be noted that considerable variability exists amongst the various legs underscoring the nonsteady nature of the wave state. Overall, the character of the vertical velocity power spectrum is quite different between the northern and southern legs and the variability between IOPs is quite large (e.g., IOPs 4 and 6).

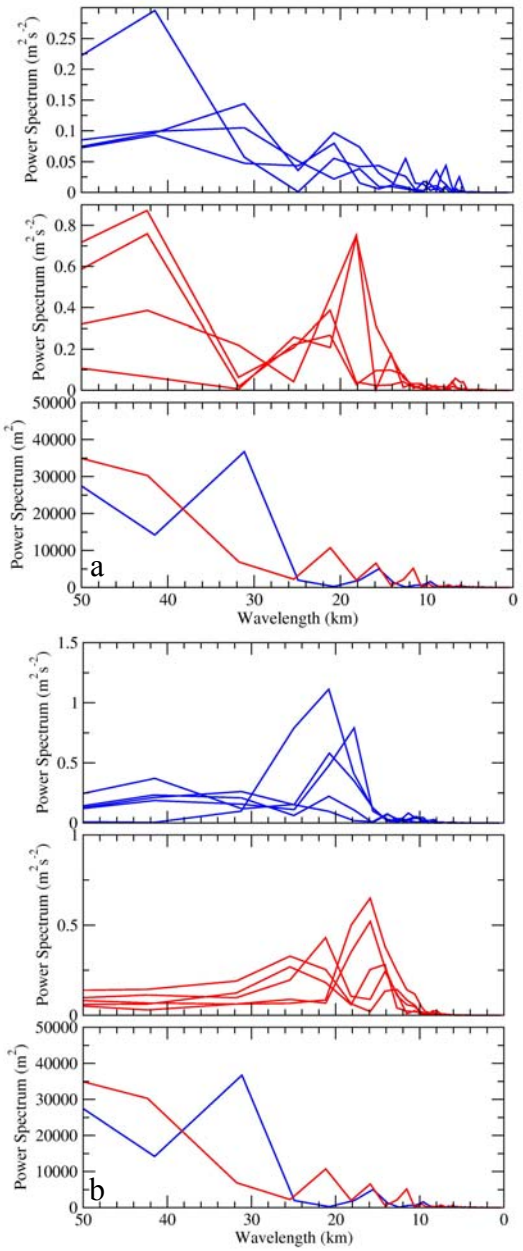

Fig. 8. The vertical velocity variance spectrum for the northern legs (top panel), southern legs (middle panel), and terrain interpolated to the flight path (bottom panel) for (a) 14 March (IOP 4) and (b) 25 March (IOP 6) at 13.1 km. The terrain spectrum along the northern leg is shown by the blue and southern leg by the red line in the bottom panels in (a) and (b).

3c. Horizontal Momentum Fluxes

The cross-mountain component of the horizontal momentum flux can be defined as,

$$M_x = \overline{\rho}\int_0^d u'w'dx,$$

where ρ is the density, u' is the cross mountain perturbation wind component and w' is the perturbation vertical velocity. The horizontal momentum flux has been computed for each of the IOPs. Significant differences exist in the horizontal momentum flux between the southern and northern legs. For example, the horizontal momentum flux for 14 March (IOP 4) is shown in Fig. 9. The momentum flux for the southern legs (middle panel) show strong negative contributions associated with the primary wave located near the middle of the Owens Valley (Fig. 3). The interpretation of the momentum flux for the northern leg is more complex with multiple waves (Fig. 3) contributing to both negative and positive maxima. Overall, the flux contribution by the primary wave is approximately greater by a factor of two for the southern leg than the northern leg. The small-scale waves located downstream of the primary wave also make significant contribution to the total momentum flux. Clearly major systematic differences are apparent over the 50 km distance separating the two legs. The accumulated momentum flux along each leg is quite steady for IOP 4 in contrast to other IOPs, which exhibited greater time variations.

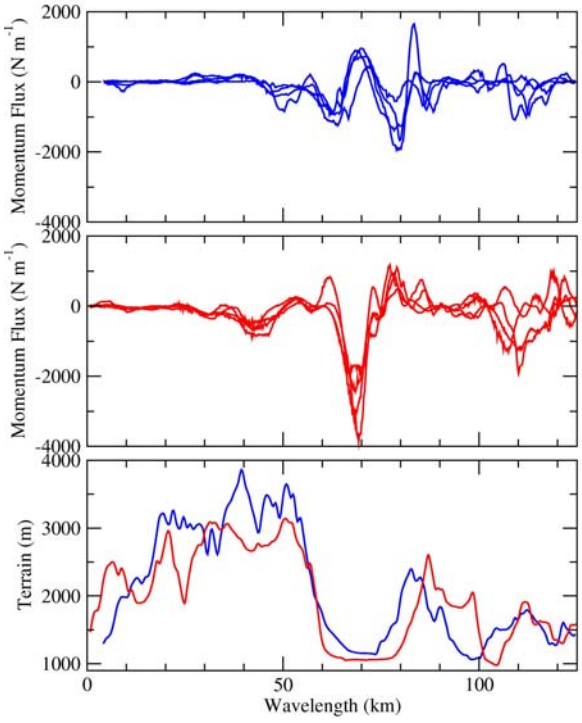

Fig. 9. The cross mountain component of the horizontal momentum flux (N m^{-1}) for the northern (blue, top panel) and southern (red, middle panel) legs for 14 March (IOP 4) at 13.1 km. The terrain (m) for the northern (blue) and southern (red) legs are shown along the bottom panel.

3d. Scatter Diagrams

Scatter diagrams were constructed based on each northern and southern flight leg pairs for a number of quantities include the maximum magnitude of the vertical velocity along the flight segment (Fig. 10) and the potential temperature variance (Fig. 11). In general, the maximum vertical velocity magnitude lies close to the diagonal. However, a number of the IOPs indicate preferential maxima along the southern (e.g., IOP 6) and northern segments (e.g., IOP 13). There appears to be less scatter in the weaker IOPs. The potential temperature variance (Fig. 11) appears to be greater along the northern flight segments for several IOPs (e.g., IOP 4, IOP 13) relative to the southern flight segment.

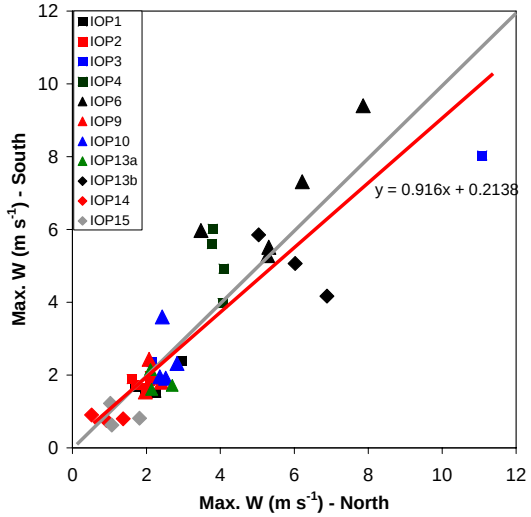

Fig. 10. Scatter diagram showing vertical velocity maximum magnitude for northern and southern leg pairs at 13.1 km.

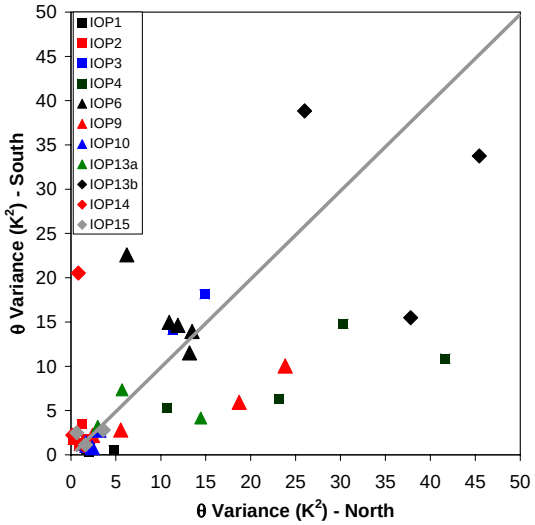

Fig. 11. Scatter diagram showing the potential temperature variance for northern and southern leg pairs at 13.1 km.

4. NUMERICAL MODEL RESULTS

The real-time 2-km horizontal resolution COAMPS 18-24 h forecasts were interpolated to the flight paths for IOP 4, 6, and 13. A comparison of the flight level and numerical model data is shown in Figs. 12a and 12b. The model appears to capture the character of the differences between the northern and southern flight segments. The model overpredicts the vertical velocity minimum associated with the primary wave in both IOPs 4 and 6 for the southern leg. Also, some phase errors are apparent in the primary wave.

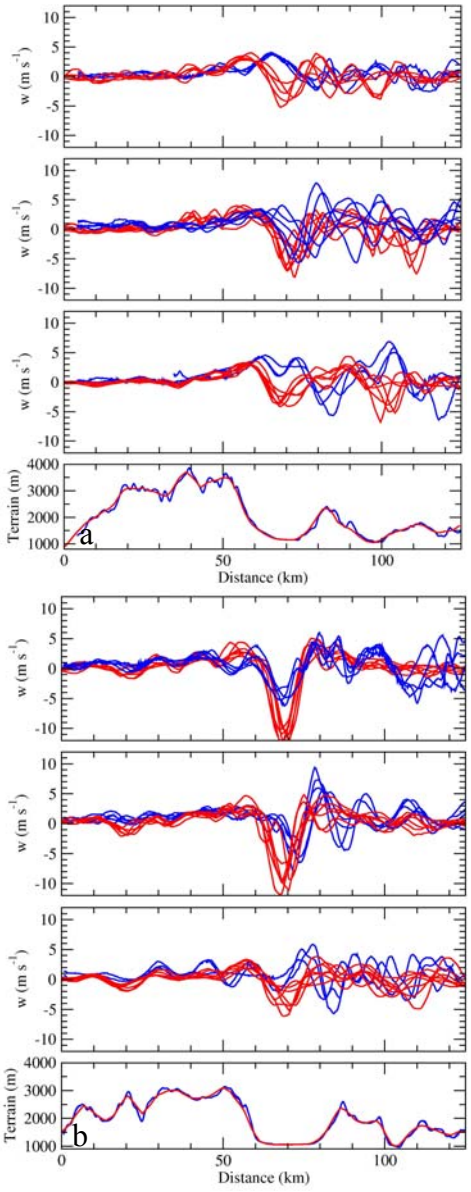

Fig. 12 Vertical velocity from the HIAPER (blue) and COAMPS (red) at 13.1 km for IOP 4 (top panel), IOP 6 (second), IOP 13 (third), and the terrain (bottom) corresponding to the (a) northern and (b) southern flight segments.

5. CONCLUSIONS AND FUTURE DIRECTIONS

Although the Sierra Nevada Range is considered nearly a two-dimensional barrier to southwesterly flow, HIAPER observations and numerical model results from T-REX indicate that the mountain waves generated by the Sierra and Inyo Ranges exhibited considerable three dimensionality. The terrain beneath the northern segment is several hundred meters higher than the southern segment, however a number of IOPs featured larger-amplitude waves on the southern leg. On the other hand, several other IOPs had larger-amplitude waves on the northern leg. The marked differences between the wave characteristics on the northern and southern flight segments is likely related to the terrain features beneath the aircraft as well as the terrain in the vicinity of the flight path.

Future observational analysis will include the BAe146 flight level data as well as the King Air cross Sierra transects. Additional high-resolution numerical modeling and linear theory will be used to quantify the role of the differences in the terrain field and the wind direction along the flight path in determining the three dimensional characteristics of mountain waves launched by the Sierras.

ACKNOWLEDGEMENTS

We gratefully acknowledge the outstanding contributions of the NCAR and T-REX staff during the T-REX field program. The research for the first author (JDD) was supported by ONR PE-0601153N. Computing time was supported by a grant of HPC time from the DoD MSRC at ASC at Wright Patterson AFB. COAMPS® is a registered trademark of the Naval Research Laboratory.

REFERENCES

Epifanio, C. C., and D. R. Durran, 2001: Three-dimensional effects in high-drag-state flows over long ridges. *J. Atmos. Sci.*, **58**, 1051–1065.

Grubišić, V., J.D. Doyle, J. Kuetter, G.S. Poulos, and C.D. Whiteman, 2004: T-REX: Terrain-Induced Rotor Experiment. *Science overview document and experiment design*. 72 pp. http://www.joss.ucar.edu/trex/documents/TREX_SOD.pdf

Hodur, R.M., 1997: The Naval Research Laboratory's Coupled Ocean/Atmosphere Mesoscale Prediction System (COAMPS). *Mon. Wea. Rev.*, **125**, 1414-1430.

Holmboe, J., and H. Klieforth, 1957: Investigations of mountain lee waves and airflow over the Sierra Nevada. Final Rep., Contract AF19(604)-728, University of California, No. 133606, Dept. of Meteorology, University of California, Los Angeles, CA, 290 pp.

Schär, C., and D. R. Durran, 1997: Vortex formation and vortex shedding in continuously stratified flows past isolated topography. *J. Atmos. Sci.*, **54**, 534–554.

Smolarkiewicz, P. K., and R. Rotunno, 1989: Low Froude number flow past three-dimensional obstacles. Part I: Baroclinically generated lee vortices. *J. Atmos. Sci.*, **46**, 1154–1164